

## THE H I ENVIRONMENT OF THREE SUPERBUBBLES IN THE LARGE MAGELLANIC CLOUD

M. S. OEY

Lowell Observatory, 1400 W. Mars Hill Rd., Flagstaff, AZ 86001, USA; oey@lowell.edu

B. GROVES

Research School of Astronomy and Astrophysics, Australian National University, Private Bag, Weston Creek  
 P.O., ACT 2611, Australia; bgroves@mso.anu.edu.au

L. STAVELEY-SMITH

Australia Telescope National Facility<sup>2</sup>, CSIRO, P.O. Box 76, Epping, NSW 1710, Australia;  
 Lister.Staveley-Smith@atnf.csiro.au

R. C. SMITH

Cerro Tololo Inter-American Observatory<sup>3</sup>, Casilla 603, La Serena, Chile; csmith@noao.edu

*Accepted to the Astronomical Journal 2001-October-09*

### ABSTRACT

The ambient interstellar environment of wind- and supernova-driven superbubbles strongly affects their evolution, but its properties are rarely well-determined. We have therefore obtained H I aperture synthesis imaging of the environment around three similar, optically-selected superbubble nebulae in the Large Magellanic Cloud. The resulting H I maps show that the ambient gas distribution around these superbubbles differ to an extreme: DEM L25 shows no neutral shell component, but is nestled within an H I hole; DEM L50 shows a massive neutral shell component, but is otherwise within an H I void; and DEM L301 shows no correspondence at all between the optical nebula and H I distribution. There is also poor correspondence between the H I and optical kinematics. These results strongly caution against inferring properties of the ambient neutral environment of individual superbubbles without direct observations. Finally, all three objects show some evidence of shock activity.

*Subject headings:* ISM: bubbles — H II regions — ISM: kinematics and dynamics — ISM: structure — supernova remnants — Magellanic Clouds

### 1. INTRODUCTION

The evolution of superbubbles created by the supernovae (SNe) and stellar winds of OB associations is a critical determinant of the structure and energetics of the interstellar medium (ISM). The coronal component of the ISM, or hot ionized medium (HIM) is believed to originate within such superbubbles and supernova remnants (SNRs; e.g., Cox & Smith 1974), hence the evolution of these structures determines whether and how this hot gas is released into the diffuse HIM. Models for the ISM are strongly dependent on whether the HIM is a pervasive, dominant component, as envisioned by e.g., McKee & Ostriker (1977), or whether it plays a lesser role as favored by, e.g., Slavin & Cox (1993), returning to a paradigm closer to the two-phase ISM of Field, Goldsmith, & Habing (1969). Superbubble evolution also directly impacts the relative volumes of enriched, coronal gas in galactic disks vs. halos (e.g., Shapiro & Field 1976). Similarly, superbubbles and their related filaments are thought to provide much of the structure for the diffuse ISM, including warm and cold H I and the warm ionized medium (e.g., Kennicutt et al. 1995). Superbubble activity is therefore fundamental to the ISM phase balance, structure, and kinematics; and it is also a principal driver of galactic evolutionary processes.

The standard model for the evolution of these superbubbles is an adiabatic, pressure-driven shell with continuous

mechanical energy injection (e.g., Pikel'ner 1968; Castor, McCray, & Weaver 1975). The mechanical power  $L$  is provided by stellar winds and SNe of the parent OB association. In this model, an outer shock sweeps up ambient ISM into a thin cooled shell, while an inner, reverse shock thermalizes the mechanical energy, thereby generating the hot interior whose pressure drives the shell growth. It is generally assumed that successive SNe can be approximated as a continuous energy injection, and that all the available SN energy is thermalized (e.g., Mac Low & McCray 1988). The standard, adiabatic model then yields simple analytic relations governing the shell evolution:

$$R \propto (L/n)^{1/5} t^{3/5} \quad , \quad (1)$$

$$v = \dot{R} \propto (L/n)^{1/5} t^{-2/5} \quad , \quad (2)$$

where  $R$  and  $v$  are the shell radius and expansion velocity, respectively,  $n$  is the ambient density, and  $t$  is elapsed time.

There are several lines of evidence supporting this standard model for superbubble evolution (see Oey 1999): a few young, stellar wind-dominated objects have well-constrained  $L$  from classification of the stellar populations, and show reasonable consistency with the predicted kinematics (Oey 1996b). In addition, multiwavelength observations of highly active star-forming regions like 30 Doradus (Wang 1999) and the starburst galaxy NGC 5253

<sup>2</sup>The Australia Telescope Compact Array is part of the Australia Telescope, which is funded by the Commonwealth of Australia for operation as a National Facility managed by CSIRO.

<sup>3</sup>National Optical Astronomy Observatories, operated by the Association of Universities for Research in Astronomy, Inc., under cooperative agreement with the National Science Foundation, U.S.A.

(Strickland & Stevens 1999) show hot gas morphologically contained within cooler shell structures. Higher ionization species like C IV and Si IV have been detected in lines of sight through all superbubbles with available observations (Chu et al. 1995), suggesting interface zones between hot and cold gas. In addition, the superbubble size distribution derived from the standard model is in remarkable agreement with observed size distributions of H I shells in the Magellanic Clouds (Oey & Clarke 1997; Kim et al. 1999).

However, other evidence suggests that superbubble evolution is often not nearly as simple as described by the standard model. The first problem is that the model overestimates the shell growth rate for young, wind-dominated superbubble nebulae (Oey 1996b; García-Segura & Mac Low 1995; Drissen et al. 1995). This could be due to a systematic underestimate in the ambient densities  $n$  by up to a factor of  $\sim 10$ , or to a similar overestimate in the input power  $L$  predicted by the assumed stellar mass-loss rates. Secondly, Oey (1996b) identified a class of superbubbles that exhibit expansion velocities that are several times higher than predicted, relative to their radii. Most of these also show anomalously bright X-ray emission, which suggests shell acceleration by SNR impacts (Chu & Mac Low 1990; Oey 1996b). In such cases, not all the available SN energy will be thermalized to power the shell expansion, thus the effect of discrete SNe on shell evolution remains unclear.

Clarifying the structure of the ambient medium is clearly essential in determining the origin of these discrepancies. Since most estimates of the ambient  $n$  for young nebular shells are based on the H $\alpha$  electron densities, the presence of a massive H I shell component could imply a significant underestimate in assumed  $n$ . Another possibility is that the structure of the ambient medium is highly irregular, providing openings to a network of low-density channels. In that case, the superbubble could be ruptured in one or more locations, depressurizing the interior and releasing hot gas into these channels. Soft X-ray imaging with *Einstein* and *ROSAT* suggests this process in at least one object, DEM L152 (Chu et al. 1993; Magnier et al. 1995) in the Large Magellanic Cloud (LMC). These minor blowouts would then cause accelerated, high-velocity kinematics in excess of the standard model predictions (e.g., Oey & Smedley 1998; Mac Low et al. 1998). Expansion into the density gradient perpendicular to galactic disks offers an additional systematic explanation for anomalously fast shell expansion in face-on galaxies (Silich & Franco 1999).

## 2. OBSERVATIONS

### 2.1. Optical narrowband imaging

In order to examine their interstellar environment in more detail, we therefore obtained H I imaging around three nebular superbubbles in the LMC. All three objects are among those found by Oey (1996b) to show anomalously high expansion velocities relative to their radii. The characteristics of these objects are summarized in Table 1: columns 1 and 2 give their identifications in the H $\alpha$  catalogs of Davies, Elliott, & Meaburn (1976) and Henize (1956), respectively; and column 3 gives the shell radius  $R$  from Oey (1996b), assuming a 50 kpc distance to the

LMC. All three objects contain OB associations in projection, and their stellar content was classified by Oey (1996a). The stars with the earliest spectral types within each superbubble are listed in column 4. Finally, column 5 lists the ratio of predicted to observed H $\alpha$  luminosity  $L_{\text{H}\alpha}(\text{pred})/L_{\text{H}\alpha}(\text{obs})$ , determined by Oey & Kennicutt (1997) from the observed stellar population.

We obtained optical narrowband imaging of these objects in the light of H $\alpha$ , [O III] $\lambda$ 5007, [S II] $\lambda$  $\lambda$ 6717,6731, and also red and green continuum. These observations were obtained from the Magellanic Clouds Emission-Line Survey (MCELS; Smith et al. 1999), which is nearing completion at the CTIO/U. Michigan 0.9-m Curtis Schmidt Telescope. The observations for DEM L301, which are also part of this survey, were published by Oey et al. (2000), and similar narrowband imaging was reported by Skelton et al. (1999). The filter bandwidths for H $\alpha$ , [O III], and [S II] are 30Å, 40Å, and 50Å, respectively, with wider continuum filters (see Smith et al. 1999); the spatial resolution is about 3–4", with 2.3" px<sup>-1</sup>. Figure 1 shows color composite images constructed from the continuum-subtracted optical narrowband observations. H $\alpha$  is shown in red, [O III] in green, and [S II] in blue. The nebular gas in all three objects is well-defined, highly circular, and filamentary. The MCELS narrowband frames of DEM L25 and DEM L50 were flux-calibrated with two longslit spectra of positions in DEM L25. These were obtained at the CTIO 1.5-m telescope on 2001 August 1 under photometric conditions.

### 2.2. H I and continuum observations

We used the Australia Telescope Compact Array (ATCA) to construct aperture synthesis imaging of these regions in the 21-cm H I line. As seen in Figure 1, DEM L25 and L50 are separated by only  $\sim 0.5^\circ$ , so for these targets we mosaicked a single field from 13 pointings. Our field for DEM L301 comprises 7 pointings. We obtained the observations in four configurations: 750A (1996 Nov 27), 750D (1997 Jan 5–7), 1.5C (1997 Sep 3), and 1.5D (1997 Mar 26–30). Excluding the data from the baselines involving antenna 6, these configurations yield 40 independent baselines ranging from 30 to 1470 m. The 21-cm line observations were carried out for an LMC heliocentric radial velocity  $v_{\text{hel}} \sim 297 \text{ km s}^{-1}$ . The bandwidth of 4 MHz was divided into 1024 channels, which were then binned to 512 channels. These correspond to a velocity coverage  $-33 < v_{\text{hel}} < 627 \text{ km s}^{-1}$ , with resolution 1.65 km s<sup>-1</sup> and sensitivity of 2.2 K. We simultaneously observed the 20-cm, 1.380 GHz continuum emission with a bandwidth of 128 MHz and full polarization information.

We observed the primary flux calibrator PKS B1934–638 at the start and end of each observing run. For phase and amplitude calibration, we observed PKS B0454–810 and PKS B0407–658. To increase the  $uv$  coverage in the shortest baselines, we also merged our data with fields from the LMC ATCA survey of Kim et al. (1998) and the Parkes single-dish survey (Staveley-Smith et al. 2001). For DEM L25 and L50, we included 50 fields from the ATCA survey, and for DEM L301, we included 37 fields. The pointing positions of our new data were adopted to coincide with the central pointings from the survey data. Altogether, these observations yield H I imaging at 50" resolution within roughly 40' of each object.

TABLE 1  
SUPERBUBBLE SAMPLE

DEM	Henize	$R(\text{pc})^a$	Sp. Type <sup>b</sup>	$L_{\text{H}\alpha}(\text{pred})/L_{\text{H}\alpha}(\text{obs})^c$
DEM L25	N185	43	O9 V	8.6
DEM L50	N186 CE	50	O6.5 V((f))	2.0
DEM L301	N70	53	O3 If*	0.2

<sup>a</sup>From Oey (1996b).

<sup>b</sup>From Oey (1996a).

<sup>c</sup>From Oey & Kennicutt (1997).

The calibration and mosaicking of the radio data were carried out with MIRIAD software. Our data were transformed to the image plane using superuniform weighting and a Gaussian taper of  $40''$ . We deconvolved the beam using a maximum entropy method, and this was then merged with the ATCA data and regridded Parkes data. We adopted a flux ratio between the Parkes data and our data of 1.2 for DEM L25 and L50, and 1.0 for DEM L301.

### 3. RESULTS

The optical emission-line properties of DEM L301 are discussed in detail by Oey et al. (2000), who also present the individual narrowband images of that object used here. Similar CCD narrowband imaging of DEM L301 was obtained and discussed by Skelton et al. (1999). In addition, Oey et al. (2000) obtained longslit spectrophotometry and compared these with tailored photoionization and shock models, showing that the observed line ratios appear to result from a combination of shock and density-bounded photoionization.

In contrast, DEM L25 and L50 emit substantially more  $\text{H}\alpha$  luminosity than apparently can be provided by the stars (Table 1). This implies an additional ionization mechanism, most plausibly shock heating. Figure 1a shows a dramatic contrast between DEM L25 and L50 in  $[\text{O III}]\lambda 5007/\text{H}\alpha \sim 0.8$ , the main shell of DEM L50 shows almost no detection in  $[\text{O III}]$ . There is some  $[\text{O III}]$  emission from the SNR N186 D, which is the small loop at the north end of DEM L50 (see §3.2 below), but Lasker (1977) cites the lack of  $[\text{O III}]$  emission in the main shell as evidence that N186 D is physically separate from the remainder of the system. The  $[\text{O III}]$  emission from DEM L25 is surprising in view of the stellar populations: DEM L25 has only a single O9 V star, whereas DEM L50 has one O6.5 V star and several late-type O stars. We would have expected  $[\text{O III}]$  emission from both nebulae, since it is even seen in H II regions dominated by O9 stars (Hunter 1992; Hunter & Massey 1990). However, the extremely low ionization parameter in these shell structures is likely to quench the photoionized  $[\text{O III}]$  emission in these objects (e.g., Oey et al. 2000; Garnett & Kennicutt 1994). The  $[\text{O III}]$  from DEM L25 is therefore most likely caused by an additional heating mechanism, probably shock excita-

tion.

The nebular kinematics of all three superbubbles have been studied extensively (e.g., Rosado et al. 1981; Lasker 1981; Dopita et al. 1981; Rosado et al. 1982; Meaburn, McGee, & Newton 1984; Rosado et al. 1990). All three show highly complex nebular velocity structure, and do not exhibit simple uniform expansion. The complex kinematics were cited as evidence consistent with the suggestion of internal SNR impacts to explain the anomalously high velocities (Oey 1996b).

Figure 2 shows the wide-angle maps of H I column density  $N(\text{H I})$  around these regions. The circles indicate the positions of the superbubbles at their approximate angular size. Figure 3 gives a closer look with composite images of the optical and H I data. Red is  $\text{H}\alpha$ , green is  $[\text{O III}]$ , and blue is now H I. It is apparent that the neutral environment varies dramatically among the three objects. DEM L25 and L50 appear to be situated in a large H I void, roughly 1.4 kpc in diameter, which apparently corresponds to the supergiant shell LMC 8 (Meaburn 1980). This structure is also clearly seen in the full H I map of the LMC constructed by Staveley-Smith et al. (2001), which combines data from the Kim et al. (1998) ATCA survey and the Parkes multibeam receiver data. Within this void, there is a patch of H I emission corresponding to DEM L50, but no apparent H I associated with DEM L25. Figure 4 shows H I maps of the region over six velocity intervals, which are the average over four channels. The mean velocity is shown in the upper left of each panel. The environment of DEM L301 (Figure 3b) shows neutral gas throughout the region in projection, but our data again show no apparent correspondence in the H I distribution with the nebular superbubble (see below). Figure 5 shows H I maps of this region averaged over five velocity channels. Hence, despite the similar appearance of the three shells in  $\text{H}\alpha$ , their H I environments are different to an extreme.

#### 3.1. DEM L25

As mentioned above, Oey & Kennicutt (1997) found that both DEM L25 and DEM L50 show more  $\text{H}\alpha$  emission than can be accounted for by the late-type O stars present within these objects. Both nebulae might therefore be expected to be radiation-bounded and associated with neutral gas. The environment of DEM L25 is con-

sistent with the superbubble being nestled within a partial H I hole (Figure 6), within a region where typically  $N(\text{H I}) \sim 1.0 \times 10^{20} \text{ cm}^{-2}$ . While some of the emission seen to the NE of DEM L25 probably belongs to an unassociated velocity component, the individual channel maps do remain consistent with general H I anticorrelation for the superbubble (Figure 4).

The H I scale height  $h$  of the LMC is dependent on radius, and difficult to determine because of the galaxy's low inclination angle. Kim et al. (1998) estimated a characteristic  $h \sim 600 \text{ pc}$ , which is weighted toward outer radii and assumes that the stars and gas are coupled. A more classical analysis by Kim et al. (1999) suggests  $h \sim 180 \text{ pc}$ , assuming stars and gas are not coupled. Elmegreen, Kim, & Staveley-Smith (2001) note a break in the H I power spectrum around a scale of  $100 \text{ pc}$ , which may also indicate a low value of  $h$ . Here we adopt a value of  $h = 300 \text{ pc}$  as a compromise estimate. If the value of  $N(\text{H I})$  found in the DEM L25 environment is characteristic of the ISM in this region, our adopted  $h$  implies an ambient volume density of  $n(\text{H I}) \sim 0.05 \text{ cm}^{-3}$ . This low value is related to the location of DEM L25 within the supergiant shell environment mentioned above.

There is no emission that unambiguously could correspond to a neutral shell of swept-up material, thus it may be that the entire shell is ionized. As seen in Figure 1, DEM L25 shows the highest excitation among the three objects, with  $[\text{O III}]\lambda 5007/\text{H}\alpha \sim 0.8$ , despite the fact that DEM L25 has the latest-type OB stars of the three nebulae. The ratio of observed to predicted  $\text{H}\alpha$  luminosity is so high,  $L_{\text{H}\alpha}(\text{obs})/L_{\text{H}\alpha}(\text{pred}) = 8.6$  (Table 1), that an additional ionization mechanism is unavoidable. This is consistent with the high  $[\text{O III}]/\text{H}\alpha$  ratio, and it is therefore less surprising to find no neutral gas component.

Figures 3a and 6 show that on the west side of DEM L25, the superbubble is interacting with an H I cloud. This is apparent both morphologically and from the enhanced optical nebular emission, indicating a density increase in the optical shell as would be expected from a collision. The  $[\text{S II}]/\text{H}\alpha$  ratio is also higher in the interaction zone, ranging around  $\sim 1.1$ , as would be expected from a ram pressure-induced shock. The mass of the H I cloud is  $\sim 1.3 \times 10^4 M_{\odot}$ , as measured within a  $230''$  box centered at 04 53 49.4,  $-70 00 12$  (J2000). Figure 7 shows an E-W position-velocity (PV) slice across the cloud, showing essentially a single component with a systemic velocity of  $240 \text{ km s}^{-1}$ . The velocity dispersion at the interaction zone is about twice as large as for the remainder of the cloud, as is qualitatively expected from a collision. The surrounding H I spatial distribution suggests that the shell is expanding into the cloud, or rather than that the entire superbubble has a systemic velocity in collision with the cloud. The standard, wind-driven evolution predicts a shell expansion velocity  $v_s \simeq 15 \text{ km s}^{-1}$ , based on the observed stellar population and shell size (Oey 1996b). This value represents a rough lower limit to the collision velocity, since  $\text{H}\alpha$  kinematic observations by Rosado et al. (1982) show much higher velocity structures that may imply  $v_s$  up to  $70 \text{ km s}^{-1}$ . We note that no kinematic features are seen in the H I observations at these high velocities, again arguing that the shell itself is fully ionized.

To the N and NE of DEM L25 is denser H I gas (Figure 3a), which is a southern extension from a major star-

forming region with high-density gas about  $300 \text{ pc}$  to the north (Figures 2a and 6). Figure 8 shows the PV diagram for a N-S slice at position 04 54 28.9,  $-69 56 21.0$ , to the NE of the shell. Two distinct kinematic components are clearly apparent around  $245$  and  $270 \text{ km s}^{-1}$ , which undoubtedly correspond to those seen in the unresolved observations by Meaburn et al. (1984). These two components are continuously present over most of the H I emission in the large mass immediately to the NE of DEM L25 and contrast with the single component of the cloud to the W. The existence of two, continuous, distinct velocity components is puzzling, but is a common feature that is also seen, for example, in the Small Magellanic Cloud (Staveley-Smith et al. 1997).

### 3.2. DEM L50

DEM L50 shows an H I configuration that is virtually inverse to that of DEM L25. DEM L50 clearly shows associated H I, plausibly in a neutral shell envelope outside the nebula, while the surrounding environment has a low density. For a single  $1.65 \text{ km s}^{-1}$  channel, our  $3\sigma$  limit is  $2.0 \times 10^{19} \text{ cm}^{-2}$ , although the effective detection limit depends on the kinematic range of the structure. Binning over four channels ( $\Delta v = 6.6 \text{ km s}^{-1}$ ) as shown in, e.g., Figure 4 gives a nominal detection limit of  $4.0 \times 10^{19} \text{ cm}^{-2}$ . This limiting ambient H I column density corresponds to a volume density of  $n(\text{H I}) \lesssim 0.02 \text{ cm}^{-3}$ , an extremely low value that is again associated with the interior of the supergiant shell environment. Figure 9 shows the excellent spatial correspondence of the  $\text{H}\alpha$  (image) and  $N(\text{H I})$  (contours) maps. The total integrated emission of  $282 \text{ Jy km s}^{-1}$  within a  $610''$  box implies a total H I mass of  $1.7 \times 10^5 M_{\odot}$  for this material. For comparison, the ambient density of  $1.4 \text{ cm}^{-3}$  estimated by Oey (1996b) and  $50 \text{ pc}$  radius imply a swept-up mass of  $1.6 \times 10^4 M_{\odot}$ . This therefore suggests that the ambient density was underestimated by an order of magnitude from the  $\text{H}\alpha$  emission. Alternatively, it may be that most of the H I originates in a structure exterior to the superbubble, although this seems unlikely because of the spatial correlation between the  $\text{H}\alpha$  and H I emission in Figure 9.

Figure 10 shows PV diagrams for E-W and N-S slices across the center of DEM L50. Most of the material has a velocity  $\sim 247 \text{ km s}^{-1}$ . The N-S slice (Figure 10a) shows a gradient to  $\sim 260 \text{ km s}^{-1}$  near the edges, suggesting that most of the central shell material may correspond to a near-side shell expansion velocity of  $v_s \sim 13 \text{ km s}^{-1}$ . Based on the observed stellar population and shell radius, the standard wind-driven evolution predicts  $v_s \sim 20 \text{ km s}^{-1}$  for the originally assumed ambient  $n = 1.4 \text{ cm}^{-3}$ , and  $v_s \sim 16 \text{ km s}^{-1}$  for  $n$  increased by an order of magnitude (Oey 1996b). Both values are consistent with a near-side H I expansion. The  $\text{H}\alpha$  velocity structure is again complex (Rosado et al. 1990); while the reported values are broadly consistent with the principal H I component around  $\sim 240 \text{ km s}^{-1}$ , it is difficult to identify the optical kinematic structures with the H I. Rosado et al. suggest a possible optical shell expansion of  $v_s \sim 25 \pm 9 \text{ km s}^{-1}$ , reasonably consistent with the tentative near-side H I expansion. However, it is also possible that the entire superbubble may have a systemic velocity offset from the ambient ISM, or that the shell kinematics are more complicated.

Figure 11 shows a PV diagram for the SNR N186 D, obtained from a N-S slice at position 05 00 12.3,  $-70$  06 22. Here we do clearly see a  $\sim 20$   $\text{km s}^{-1}$  line splitting over a region extending about  $4'$ . However, this is puzzlingly inconsistent with  $\text{H}\alpha$  observations suggesting  $v_s \sim 90$   $\text{km s}^{-1}$  for the SNR, found in the  $\text{H}\alpha$  Fabry-Pérot data of Laval et al. (1989). Their data generally appear to show two components around 160 and 320  $\text{km s}^{-1}$ , and there are no reported velocity structures in the range 240 to 270  $\text{km s}^{-1}$ , which are seen in our H I observations. Our data cube has limiting extremes of 190 and 336  $\text{km s}^{-1}$ , so we cannot adequately probe the same kinematic range as the optical data, but we detect no structures near these extremes in our cube, within our effective detection limit of  $\sim 4 \times 10^{19}$   $\text{cm}^{-2}$ .

### 3.3. DEM L301

The H I environment of DEM L301 is still different in character from either that of DEM L25 or DEM L50. As seen in Figure 12, there is no apparent correspondence at all between the H I emission and nebular emission, whether as a correlation or anticorrelation. Nor can we identify any correspondence in the individual channel maps, (Figure 5). Figure 13 shows PV diagrams for E-W and N-S slices across the center of the optical nebula. There is no kinematic structure readily identifiable with the superbubble either. Optically, DEM L301 again shows complex, high-velocity components in  $\text{H}\alpha$ , with velocity differences up to 100  $\text{km s}^{-1}$  (Rosado et al. 1981). Since the object is density-bounded and leaking ionizing photons (Table 1), the shell is probably fully ionized, which helps explain the lack of corresponding H I structure. However, this would still imply that the H I distribution is clumpy or patchy, to explain the absence of an H I hole. Typically in this region  $N(\text{H I}) \sim 1.3 \times 10^{21}$   $\text{cm}^{-2}$ , suggesting a mean volume density of 0.7  $\text{cm}^{-3}$ .

### 4. 20-CM CONTINUUM OBSERVATIONS

Our 20-cm (1380 MHz) continuum observations of the three superbubbles show excellent spatial correspondence with the  $\text{H}\alpha$  distributions, as expected for the nebular thermal continuum. We measure flux densities within our 128 MHz bandwidth of  $84 \pm 17$  mJy and  $173 \pm 35$  mJy for DEM L25 and DEM L301, respectively, excluding point sources. The flux density of DEM L50, excluding one point source, is  $229 \pm 46$  mJy, of which  $99 \pm 20$  mJy corresponds to the SNR in the northern region.

Since all three superbubbles have been suggested to be affected by shocks, there may be a non-negligible contribution to the continuum from non-thermal emission. To evaluate this possibility, we constructed spectral index maps using our 1380 MHz data and 843 MHz data from the Molonglo Observatory Synthesis Telescope (MOST) survey of the Magellanic Clouds (Turtle et al. 1998). The results are noisy, but broadly suggest that DEM L25 and the SNR N186 D in DEM L50 have spectral indices roughly around  $\alpha \sim -0.8$  for flux density  $S \propto \nu^\alpha$ , whereas DEM L301 and the remainder of DEM L50 have lower spectral indices  $\alpha \sim -0.3$ . This is consistent with the stronger shock signatures seen for DEM L25 and SNR N186 D, specifically, the higher  $[\text{O III}]/\text{H}\alpha$ ,  $[\text{S II}]/\text{H}\alpha$ , overproduction of  $\text{H}\alpha$ , and higher-velocity kinematics. The data thus qualitatively suggest the presence of some non-thermal emission

for at least DEM L25 and SNR N186 D. These results are consistent with the spectral indices reported by Filipović et al. (1998) in their multi-band radio continuum survey. For DEM L25 and DEM L50 (unresolved), they obtain  $\alpha = -0.67 \pm 0.09$  and  $\alpha = -0.73 \pm 0.19$ , respectively, while for DEM L301 they find  $\alpha = -0.02 \pm 0.03$ . These values may be compared to the mean  $\alpha = -0.15$ , standard deviation  $\sigma = 0.31$  for H II regions; and mean  $\alpha = -0.43$ ,  $\sigma = 0.19$  for SNRs, reported by the Filipović et al. (1998) survey.

### 5. CONCLUSION

We have obtained H I observations of the environment around three optically-selected superbubbles in the LMC. The optical nebulae have similar properties: all are roughly 50 pc in radius and show optical kinematic structures with anomalously high expansion velocities that contrast with values expected from the standard evolutionary model for wind and SN-generated superbubbles. We find that the H I environment within roughly 500 pc of the objects vary to an extreme. DEM L25 shows no H I associated with the superbubble itself, but appears to be nestled within an H I hole, and the shell is interacting with an adjacent H I cloud; DEM L50 shows an H I component to the shell that is  $\sim 10$  times more massive than the ionized shell, but is otherwise in a large H I void; and DEM L301 shows no correlation of any kind between the optical and H I distributions. Furthermore, the high-velocity kinematics observed optically for all three objects are not seen in any of our H I data. These findings strongly caution against inferring properties of the neutral interstellar environment around any individual superbubbles without direct observations.

All three superbubbles have reported signatures suggestive of shock activity, including supersonic nebular velocities. DEM L25 and DEM L50 show elevated  $\text{H}\alpha$  emission in excess of that predicted from photoionization by their classified stellar populations, and DEM L50 encompasses the known SNR N186 D on its northern edge. DEM L25 also shows elevated  $[\text{O III}]/\text{H}\alpha$  and all objects show high  $[\text{S II}]/\text{H}\alpha$ . The emission-line spectrum of DEM L301 was modeled in detail by Oey et al. (2001), who found evidence of contributions by shock excitation. We examined our 1380 MHz (20 cm) continuum in conjunction with 843 MHz continuum observations from the MOST survey to obtain rough, spatially-resolved estimates of the spectral indices. These suggest some presence of a non-thermal component for at least DEM L25 and the SNR N186 D.

We mentioned above that the new H I data do not show the complex, high-velocity shell components that are evident in the optical nebular data for these objects. However, the uneven H I distributions for DEM L25 and DEM L301 are consistent with the high ionization state of these nebulae, suggesting that these shells are fully ionized. Their patchy H I remains consistent with the optical filaments corresponding to incipient blowout features or material accelerated by SNR impacts, as has been previously suggested. The lack of correspondence between the nebular and H I kinematics is more problematic for DEM L50, although the dominant  $\text{H}\alpha$  and H I components are broadly consistent with each other. The H I velocity profile suggests that the neutral component may correspond to the approaching side of the shell.

We gratefully acknowledge Anne Green for providing the MOST survey data, and Sung Kim for assistance during one of our observing runs. MSO thanks the ATNF/CSIRO for warm hospitality through their Distinguished Visitor

Programme. Some of this work was carried out by MSO while at the Institute of Astronomy, Cambridge and the Space Telescope Science Institute. We also thank the referee, Margarita Rosado, for her helpful suggestions.

## REFERENCES

- Castor, J. I., McCray, R., & Weaver, R., 1975, *ApJL*, 200, L107  
 Chu, Y.-H. & Mac Low, M.-M., 1990, *ApJ*, 365, 510  
 Chu, Y.-H., Mac Low, M.-M., García-Segura, G., Wakker, B., & Kennicutt, R. C. 1993, *ApJ*, 414, 213  
 Cox D. P. & Smith B. W. 1974, *ApJL*, 189, L105  
 Davies, R. D., Elliott, K. H., & Meaburn, J., 1976, *Mem. RAS*, 81, 89  
 Dopita, M. A., Ford, V. L., McGregor, P. J., Mathewson, D. S., & Wilson, I. R., 1981, *ApJ*, 250, 103  
 Drissen L., Moffat A. F. J., Walborn N. R., & Shara M. R. 1995, *AJ*, 110, 2235  
 Elmegreen, B. G., Kim, S., & Staveley-Smith, L., 2001, *ApJ*, in press; astro-ph/0010578  
 Field G. B., Goldsmith D. W., & Habing H. J. 1969, *ApJL*, 155, L149  
 Filipović, M. D., Haynes, R. F., White, G. L., & Jones, P. A., 1998, *A&AS*, 130, 421  
 García-Segura G. & Mac Low M.-M. 1995, *ApJ*, 455, 145  
 Garnett, D. R. & Kennicutt, R. C., 1994, *ApJ*, 426, 123  
 Henize, K. G., 1956, *ApJS*, 2, 315  
 Hunter 1992, *ApJS*, 79, 469  
 Hunter & Massey 1990, *AJ*, 99, 846  
 Kennicutt R. C., Bresolin F., Bomans D. J., Bothun G. D., & Thompson I. B. 1995, *AJ*, 109, 594  
 Kim, S., Dopita, M. A., Staveley-Smith, L., & Bessell, M. S., 1999, *AJ*, 118, 2797  
 Kim, S., Staveley-Smith, L., Dopita, M. A., Freeman, K. C., Sault, R. J., Kesteven, M. J., & McConnell, D., 1998, *ApJ*, 503, 674  
 Lasker, B. M., 1977, *PASP*, 89, 474  
 Lasker, B. M., 1981, *PASP*, 93, 422  
 Laval, A., Rosado, M., Boulesteix, J., Georgelin, Y. P., Marcelin, M., Monnet, G., & Le Coarer, E., 1989, *A&A*, 208, 230  
 Mac Low M.-M. & McCray R. 1988, *ApJ*, 324, 776  
 Mac Low M.-M., Chang, T. H., Chu, Y.-H., Points, S. D., Smith, R. C., & Wakker, B. P., 1998, *ApJ*, 493, 260  
 Magnier E. A., Chu Y.-H., Points S. D., Hwang U., & Smith R. C. 1996, *ApJ*, 464, 829  
 McKee C. F. & Ostriker J. P. 1977, *ApJ*, 218, 148  
 Meaburn, J., 1980, *MNRAS*, 192, 356  
 Meaburn, J., McGee, R. X., & Newton, L. M., 1984, *MNRAS*, 206, 705  
 Oey, M. S., 1996a, *ApJ*, 465, 231  
 Oey, M. S., 1996b, *ApJ*, 467, 666  
 Oey, M. S., 1999, in *New Views of the Magellanic Clouds*, IAU Symp. 190, eds. Y.-H. Chu, N. Suntzeff, J. Hesser, & D. Bohlender, (San Francisco: ASP), 78  
 Oey, M. S. & Clarke, C. J. 1997, *MNRAS*, 289, 570  
 Oey, M. S., Dopita, M. A., Shields, J. C., & Smith, R. C., 2000, *ApJS*, 128, 511  
 Oey, M. S. & Kennicutt, R. C., 1997, *MNRAS*, 291, 827  
 Oey, M. S. & Smedley, S. A., 1998, *AJ*, 116, 1263  
 Pikel'ner S. B. 1968, *Astrophys. Lett.* 2, 97  
 Rosado, M., Georgelin, Y. M., Georgelin, Y. P., Laval, A., & Monnet, G., 1981, *A&A*, 97, 342  
 Rosado, M., Georgelin, Y. M., Georgelin, Y. P., Laval, A., & Monnet, G., 1982, *A&A*, 115, 61  
 Rosado, M., Laval, A., Boulesteix, J., Georgelin, Y. P., Greve, A., Marcelin, M., Le Coarer, E., & Viale, A., 1990, *A&A*, 238, 315  
 Shapiro, P. R. & Field, G. B., 1976, *ApJ*, 205, 762  
 Silich, S. A. & Franco, J., 1999, *ApJ*, 522, 863  
 Skelton, B. P., Waller, W. H., Gelderman, R. F., Brown, L. W., Woodgate, B. E., Caulet, A., & Schommer, R. A., 1999, *PASP*, 111, 465  
 Slavin J. D. & Cox D. P. 1993, *ApJ*, 417, 187  
 Smith, R. C., et al., 1999, in *New Views of the Magellanic Clouds*, IAU Symp. 190, eds. Y.-H. Chu, N. Suntzeff, J. Hesser, & D. Bohlender, (San Francisco: ASP), 28  
 Staveley-Smith, L., Kim, S., Calabretta, M. R., Haynes, R. F., Kesteven, M. J., & Wilson, W. E., 2001, *MNRAS*, submitted  
 Staveley-Smith, L., Sault, R. J., Hatzidimitriou, D., Kesteven, M. J., & McConnell, D., 1997, *MNRAS*, 289, 225  
 Strickland, D. K. & Stevens, I. R., 1999, *MNRAS*, 306, 43  
 Turtle, A. J., Ye, T., Amy, S. W., & Nicholls, J., 1998, *PASA*, 15, 280  
 Wang, Q. D., 1999, *ApJL*, 517, L27

FIG. 1.— Composite narrow-band images of *a*) DEM L25 and DEM L50; and *b*) DEM L301.  $H\alpha$  is shown in green, [O III] in blue, and [S II] in red. Figure 1 is constructed from the continuum-subtracted images with arbitrary intensity scaling. Beware that the relative intensities of the three bands vary between the two fields. North is up, east to the left; see Figures 2, 6, 9, and 12 for angular scale.

FIG. 2.— H I column density maps of the environment around *a*) DEM L25 and DEM L50; and *b*) DEM L301. The circles roughly indicate the position and size of the objects, with DEM L25 on the west side of Figure 2*a*.

FIG. 3.— Composite images of *a*) DEM L25 and *b*) DEM L50, with  $H\alpha$  shown in red, [O III] in green, and H I in blue, using arbitrary intensity scaling.

FIG. 4.— H I maps of the region around DEM L25 and L50. Each panel shows the average of four channels, whose mean heliocentric velocity in  $\text{km s}^{-1}$  is shown in the upper left. The circles indicate the positions of DEM L25 and L50, with the former on the west side.

FIG. 5.— H I maps for the region around DEM L301. Each panel shows the average of five velocity channels.

FIG. 6.—  $N(\text{H I})$  contour map of DEM L25, superimposed on  $H\alpha$ . Contour intervals are  $2 \times 10^{20} \text{ cm}^{-2}$ , beginning at  $2 \times 10^{19} \text{ cm}^{-2}$ .

FIG. 7.— Position-velocity diagram oriented E-W across the cloud to the W of DEM L25. The center is at 04 53 14.7,  $-69\ 59\ 35$ , with E to the left (negative offsets).

FIG. 8.— Position-velocity diagram for the H I mass NE of DEM L25, centered at 04 54 29.9,  $-69\ 55\ 35$  (J2000). N is to the left (negative offsets).

FIG. 9.—  $N(\text{H I})$  contour map of DEM L50, superimposed on  $H\alpha$ . Contours are as in Figure 6.

FIG. 10.— Position-velocity diagrams across the center of DEM L50, oriented *a*) E-W; and *b*) N-S. E and N are to the left (negative offsets).

FIG. 11.— Position-velocity diagram across the SNR N186 D. The slice is oriented N-S, centered at 05 00 12.3,  $-70\ 06\ 23$  (J2000), with N shown to the left.

FIG. 12.—  $N(\text{H I})$  contour map of DEM L301, superimposed on  $H\alpha$ . Contour intervals are  $3 \times 10^{20} \text{ cm}^{-2}$ , beginning at  $2 \times 10^{19} \text{ cm}^{-2}$ .

FIG. 13.— Position-velocity diagram across the center of DEM L301, oriented *a*) E-W; and *b*) N-S. E and N are shown to the left.

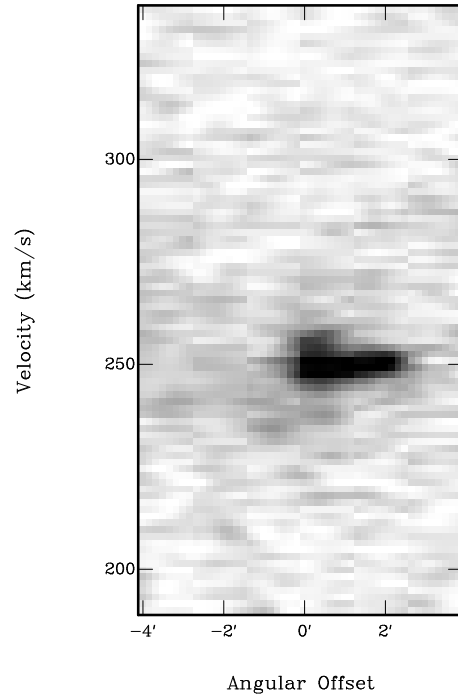


FIG. 7.—

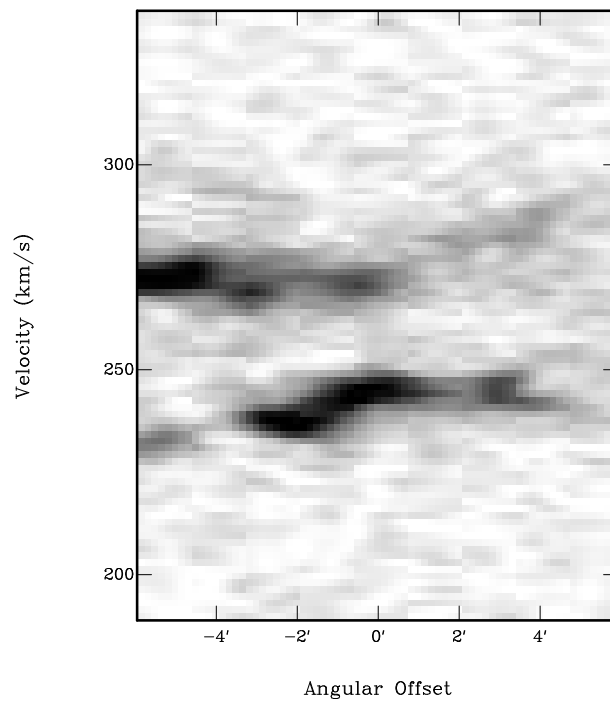


FIG. 8.—

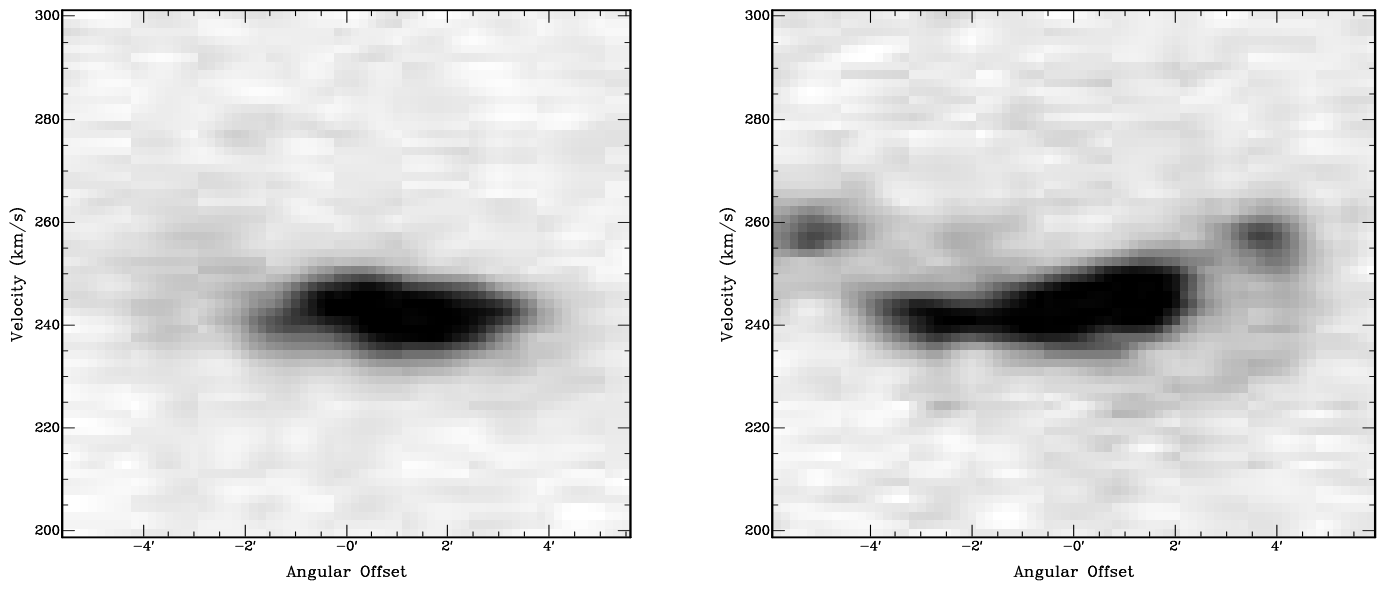


FIG. 10.— *a* and *b*

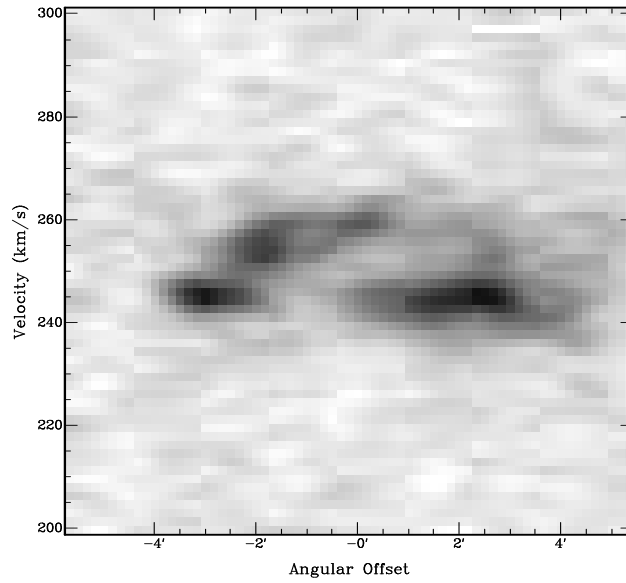
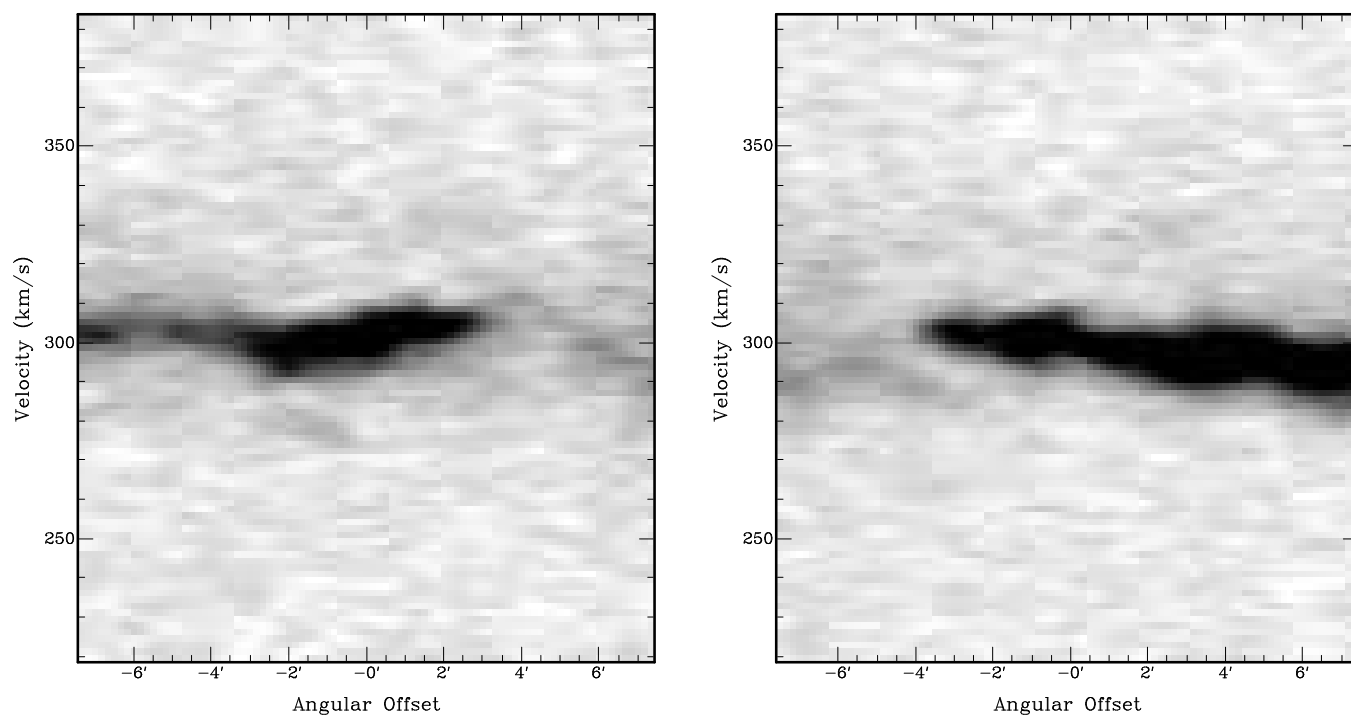


FIG. 11.—

FIG. 13.— *a* and *b*

This figure "Oey\_f1a.jpg" is available in "jpg" format from:

<http://arxiv.org/ps/astro-ph/0112057v1>

This figure "Oey\_f1b.jpg" is available in "jpg" format from:

<http://arxiv.org/ps/astro-ph/0112057v1>

This figure "Oey\_f2a.jpg" is available in "jpg" format from:

<http://arxiv.org/ps/astro-ph/0112057v1>

This figure "Oey\_f2b.jpg" is available in "jpg" format from:

<http://arxiv.org/ps/astro-ph/0112057v1>

This figure "Oey\_f3a.jpg" is available in "jpg" format from:

<http://arxiv.org/ps/astro-ph/0112057v1>

This figure "Oey\_f3b.jpg" is available in "jpg" format from:

<http://arxiv.org/ps/astro-ph/0112057v1>

This figure "Oey\_f4.jpg" is available in "jpg" format from:

<http://arxiv.org/ps/astro-ph/0112057v1>

This figure "Oey\_f5.jpg" is available in "jpg" format from:

<http://arxiv.org/ps/astro-ph/0112057v1>

This figure "Oey\_f6.jpg" is available in "jpg" format from:

<http://arxiv.org/ps/astro-ph/0112057v1>

This figure "Oey\_f9.jpg" is available in "jpg" format from:

<http://arxiv.org/ps/astro-ph/0112057v1>

This figure "Oey\_f12.jpg" is available in "jpg" format from:

<http://arxiv.org/ps/astro-ph/0112057v1>